AIMS Mathematics, 10(9): 20443–20465.
DOI: 10.3934/math.2025913
Received: 05 May 2025
Revised: 23 August 2025
Accepted: 25 August 2025
Published: 05 September 2025

https://www.aimspress.com/journal/Math

Research article

Statistical quantifiers and nonlinear conservative-dissipative classical transition

Gaspar Gonzalez Acosta[1,2] **and Andrés M. Kowalski**[1,2,*]

[1] Instituto de Física La Plata-CONICET/UNLP, 1900, Buenos Aires, Argentina
[2] Comision de Investigaciones Científicas (CIC)

* **Correspondence:** Email: kowalski@fisica.unlp.edu.ar.

Abstract: We investigated the dynamics of a regular nonlinear semiclassical system by employing Shannon entropy together with two associated formulations of statistical complexity: the López-Ruiz–Mancini–Calbet (LMC) and Jensen–Shannon approaches. Additionally, Tsallis entropy was used as an alternative quantifier. In this context, quantum variables interacted with a classical environment, and both conservative and dissipative regimes were considered. To compute information-theoretic quantifiers, probability distributions were extracted from the system's temporal evolution using the Bandt–Pompe permutation method. The classical limit was characterized by a motion invariant linked to the uncertainty principle. Our analysis revealed three distinct zones that characterized the structure of transitions across the classical–quantum boundary. These findings confirmed earlier results obtained in markedly different dynamical systems. This consistency supported the idea of a possible generalization, which, if established, would have significant implications for both semiclassical and quantum theories.

Keywords: quantum-classical interaction; conservative and dissipative regimes; classical limit; statistical complexity; Bandt-Pompe method

1. Introduction

It is well known that the emergence of classical behavior from quantum mechanics has become a topic of significant interest in recent years. This interest spans theoretical approaches such as Bohmian analyses and semiclassical quantization schemes [1, 2], studies of the boundary between classical and quantum physics [3], and research on the emergence of classical particles from the quantum domain [4].

On the experimental side, quantum-to-classical transitions have been demonstrated in optomechanical systems [5], cavities [6], and superconducting circuits [7]. One of the key

mechanisms involved is the decoherence process [8], which plays a central role in the suppression of quantum coherence and the emergence of classical dynamics. This phenomenon is closely connected to mesoscopic physics, a subfield concerned with systems of intermediate size.

Devices used in nanotechnology are representative examples of mesoscopic systems, where quantum phenomena such as phase coherence, collective effects, and phase transitions play a fundamental role. In this area, research has been investigated into the general principles of transport and mesoscopic fluctuations [9], coherent optical dynamics in quantum dots and nanostructures [10], and phase transitions in finite-size quantum systems [11].

At the same time, semiclassical approaches have long played a key role in the description of physical phenomena. A wide variety of strategies have been developed and applied in diverse contexts, including nuclear spin precession in magnetic fields [12]; nonlinear optics and chaos in laser–matter interaction [13]; hybrid formulations of quantum–classical systems for studying coupling mechanisms [14]; and modeling the interaction between classical and quantum particles [15]. Further developments include semiclassical approximations tailored to chaotic or dissipative systems [16, 17], the construction of classical analogs for fermionic dynamics [18], the treatment of exceptional points in non-Hermitian settings [19], semiclassical expansions in atom–field interaction models [20], interpretational perspectives on quantum–classical correspondence [21], mechanisms for the emergence of chaos [22], and analytical derivations of characteristic quantum time scales [23].

In previous studies, we have analyzed systems in which quantum and classical variables coexist [24]. The classical variables typically represent an environment or reservoir that interacts with the quantum subsystem [25, 26].

Within this framework, the classical limit of quantum systems has been investigated using a motion-invariant formulation related to the uncertainty principle [24]. Our prior work has addressed this problem dynamically [25, 26] and through various techniques drawn from information theory (IT) [27].

The particular semiclassical system analyzed in this paper was previously studied in [26] through Poincaré sections and by monitoring the time evolution of relevant observables. Two regimes were considered: the conservative case and, for the first time, the dissipative one. In the present work, the system is revisited by initially employing Shannon entropy in combination with two established approaches to statistical complexity: López-Ruiz, Mancini, and Calbet complexity (LMC complexity), and a Jensen–Shannon-based formulation. The foundational work by López-Ruiz et al. [28] introduced a statistical measure of complexity based on the interplay between entropy and disequilibrium, later applied to various physical systems [29] and extended to nonequilibrium contexts [30]. Jensen–Shannon complexity [31] employs a distinct metric structure in probability space. Lamberti et al. [31] proposed an intensive entropic non-triviality measure, and Martin et al. [32] further explored its generalized geometrical and analytical properties. Additionally, we employ the generalized Tsallis entropy [33].

To evaluate these quantifiers, a probability distribution function is required. The Bandt–Pompe permutation-based symbolic method [34] is employed, which has demonstrated effectiveness in capturing essential features of diverse time series [35, 36].

Our goal is to understand and characterize the underlying process, extracting insights that may remain inaccessible through dynamical tools alone. The behavior of numerous Poincaré sections, represented through a single suitable information-theoretic quantifier, facilitates the characterization

of the process. This approach enables the identification of trends across the full range of the parameter E_r, including asymptotic behaviors that may be overlooked in a purely dynamical analysis.

First, we aim to verify whether the process exhibits the structural zones and the convergence toward the classical outcome described in [26]. Second, upon confirmation, we pursue a more efficient analysis of the boundaries between zones. We quantitatively determine the limits of these regions through threshold analysis and the use of first and second numerical derivatives. Additionally, we identify the presence of secondary critical points.

The three dynamical zones in the classical limit described in [26] coincide with those found in the classical limit of systems with markedly different dynamics, including chaotic behavior. If these zones are also confirmed in the present work, where the system exhibits regular conservative and dissipative dynamics, this would support the idea of a possible generalization. If such a generalization is established, it could have meaningful implications for both semiclassical and quantum domains.

The manuscript is organized as follows. Section 2 presents the specific semiclassical system analyzed in this work along with our approach to the classical limit. In Section 3, we provide a brief overview of the Bandt–Pompe method. Section 4 summarizes the topic of information-theoretic quantifiers. In Section 5, we present selected dynamical results. Section 6 contains the main findings of this study. Conclusions are discussed in Section 7. Finally, two appendices are included: Appendix A describes the general semiclassical methodology, while Appendix B presents a demonstration of an inequality related to the uncertainty principle.

2. Semiclassical model and the classical limit

We consider a Hamiltonian of the form

$$\hat{H} = \frac{1}{2}\left(\omega_q\left(\hat{x}^2 + \hat{p}^2\right) + \omega_{cl}\left(A^2 + P_A^2\right)\hat{I} + e_q^{cl}A^2\hat{x}^2\right). \tag{2.1}$$

In this Hamiltonian, $\hat{x}$ and $\hat{p}$ are considered quantum operators, while A and P_A are canonically conjugated classical variables. $\hat{I}$ is the identity operator. ω_q and ω_{cl} are frequencies, and e_q^{cl} is a positive parameter [24]. The nonlinear quantum–classical interaction appears through the term $e_q^{cl}A^2\hat{x}^2$ in (2.1). The semiclassical methodology we use is developed in the Appendix A. The equations of motion that govern the system, as demonstrated in [26], are given by the following set of coupled nonlinear equations:

$$\frac{d\langle\hat{x}^2\rangle}{dt} = \omega_q\langle\hat{L}\rangle, \tag{2.2a}$$

$$\frac{d\langle\hat{p}^2\rangle}{dt} = -\left(\omega_q + e_q^{cl}A^2\right)\langle\hat{L}\rangle, \tag{2.2b}$$

$$\frac{d\left\langle\hat{L}\right\rangle}{dt} = 2\left(\omega_q\left\langle\hat{p}^2\right\rangle - \left(\omega_q + e_q^{cl}A^2\right)\left\langle\hat{x}^2\right\rangle\right), \tag{2.2c}$$

$$\frac{dA}{dt} = \omega_{cl}P_A, \tag{2.2d}$$

$$\frac{dP_A}{dt} = -A\left(\omega_{cl} + e_q^{cl}\left\langle\hat{x}^2\right\rangle\right) - \eta P_A, \tag{2.2e}$$

where, if $\eta > 0$, our system is dissipative. The operator $\hat{L}$ is defined as $\hat{L} = \hat{x}\hat{p} + \hat{p}\hat{x}$. To study the classical limit of system (2.2), we compare it with the solutions corresponding to the classical analogue of Hamiltonian (2.1) [25]

$$H = \frac{1}{2}\left(\omega_q\left(x^2 + p^2\right) + \omega_{cl}\left(A^2 + P_A^2\right) + e_q^{cl}A^2x^2\right). \tag{2.3}$$

By Hamilton's equations, as shown in the Appendix A, we obtain

$$\frac{dx^2}{dt} = \omega_q L, \tag{2.4a}$$

$$\frac{dp^2}{dt} = -\left(\omega_q + e_q^{cl}A^2\right)L, \tag{2.4b}$$

$$\frac{dL}{dt} = 2\left(\omega_q p^2 - \left(\omega_q + e_q^{cl}A^2\right)x^2\right), \tag{2.4c}$$

$$\frac{dA}{dt} = \omega_{cl}P_A, \tag{2.4d}$$

$$\frac{dP_A}{dt} = -A\left(\omega_{cl} + e_q^{cl}x^2\right) - \eta P_A, \tag{2.4e}$$

for the classical variables $(x^2(t), p^2(t), L(t))$ and $L = 2xp$.

We define I as

$$I = \langle\hat{x}^2\rangle\langle\hat{p}^2\rangle - \frac{\langle\hat{L}\rangle^2}{4} \geq \frac{\hbar^2}{4}. \tag{2.5}$$

The quantity I is a motion invariant of system (2.2) in both the conservative and dissipative regimes [24, 26], i.e., $dI/dt = 0$, and is directly related to the uncertainty principle. The inequality is derived in Appendix B. This quantity characterizes the deviation from classical behavior, with the condition $I = x^2p^2 - L^2/4 = 0$ corresponding to a trivial invariant. It should be noted that we focus on the temporal evolution of the quantum mean values $\langle\hat{x}^2\rangle(t)$, $\langle\hat{p}^2\rangle(t)$, and $\langle\hat{L}\rangle(t)$, as it represents the minimal collection of observables that contain information on the uncertainty principle through the invariant I [26].

Equations (2.2) do not explicitly depend on $\hbar$, while mean values depend on it via the initial conditions, through I, satisfying (2.5). The inequality (2.5), and its classical value, are crucial in our study of the classical limit $I \to 0$, as will be seen throughout the article.

Now, let us focus on the relative energy E_r

$$E_r = \frac{|E|}{I^{1/2}\omega_q}. \tag{2.6}$$

Here, $E = \langle H\rangle$ denotes the total energy, and E_r is a dimensionless parameter that serves as a reliable measure of quantumness. It remains invariant in the conservative regime. This is a necessary condition, since any quantity extracted from the time series is associated with a fixed value of the parameter in question.

In the dissipative regime, energy is not conserved; the natural generalization is to replace E in (2.6) with its initial value $E(0)$ [26], ensuring that E_r remains a motion invariant. Inequality $E_r \geq 1$, which follows from the uncertainty principle, defines a lower bound for the relative energy. The equality case, $E_r = 1$, corresponds to fully quantum dynamics. The classical limit is attained when $I \to 0$, that is,

$$E_r \to \infty. \tag{2.7}$$

3. Bandt-Pompe method

To calculate our information quantifiers, it is necessary to have a probability distribution associated with the data series to be analyzed. In this case, it corresponds to a time series of the semiclassical and classical systems.

We obtain this probability distribution function (PDF) using the Bandt–Pompe method [34]. This methodology consists of a symbolization process described as follows. Let $\{x_t\}_{t=1,2,\cdots,N}$ be an arbitrary time series. The first step is to divide it into $n = N - (d-1)\tau$ overlapping partitions, each comprising $d > 1$ observations separated by $\tau \geq 1$ time units. For given values of d and τ, each data partition can be represented as

$$w_p = \left(x_p, x_{p+\tau}, x_{p+2\tau}, \cdots, x_{p+(d-2)\tau}, x_{p+(d-1)\tau}\right), \tag{3.1}$$

where $p = 1, 2, \cdots, n$ is the partition index.

The Bandt-Pompe approach depends solely on two parameters: the embedding dimension d and the embedding delay τ. Initially, Bandt and Pompe considered only the case $\tau = 1$, which corresponds to partitions formed by successive elements of the time series. Subsequent contributions expanded this framework to allow delays $\tau > 1$ [37, 38].

Given a partition w_p, the associated permutation $\pi_p = (r_0, r_1, \ldots, r_{d-1})$ is constructed by reordering the index set $(0, 1, \ldots, d-1)$ according to the values of the elements in w_p. More precisely, the indices are arranged such that $x_{p+r_0} \leq x_{p+r_1} \leq \cdots \leq x_{p+r_{d-1}}$. When two elements are equal, their relative index order is preserved; that is, if $x_{p+r_{k-1}} = x_{p+r_k}$, then necessarily $r_{k-1} < r_k$ [34, 38].

The symbolic sequence $\{\pi_p\}_{p=1,2,\ldots,n}$ is then constructed from the permutation symbols corresponding to all partitions.

The ordinal probability distribution $P = \{p_i(\Pi_i)\}_{i=1,2,\cdots,n_\pi}$ is constructed by assigning to each admissible permutation Π_i its relative frequency of occurrence within the symbolic sequence:

$$p_i(\Pi_i) = \frac{\text{number of partitions of type } \Pi_i \text{ in } \{\pi_p\}}{n}. \tag{3.2}$$

The Bandt–Pompe method has several desirable features: (i) simplicity, (ii) extremely fast computation, and (iii) robustness. In addition, it is invariant under nonlinear monotonic transformations. This method can be applied to any type of time series (regular, chaotic, noisy, or experimental) [27].

4. Information quantifiers

This section presents basic concepts concerning the information quantifiers employed.

4.1. Shannon permutation entropy

Shannon permutation entropy is defined as follows:

$$S\,(P) = -\sum_{i=1}^{n_\pi} p_i\,(\Pi_i) \log p_i\,(\Pi_i), \tag{4.1}$$

where the probability distribution $P = \{p_i\,(\Pi_i)\}_{i=1,2,\cdots,n_\pi}$ is obtained using the Bandt and Pompe method. Permutation entropy quantifies the randomness in the ordering dynamics of a time series. This means

that $S = 0$ implies regular behavior, while $S = \log(n_\pi)$ indicates behavior with maximum disorder [34, 38].

The normalized permutation entropy adopts the form

$$H(P) = \frac{S(P)}{S_{\max}}, \tag{4.2}$$

where $S_{\max} = \log(n_\pi)$ denotes the entropy of the uniform distribution. The normalized entropy H satisfies $0 \leq H \leq 1$.

4.2. LMC statistical complexity

In 1995, López-Ruiz, Mancini, and Calbet (LMC) [28], proposed a measure of complexity given by the following expression:

$$C_{LMC} = H(P) \cdot D(P, P_e), \tag{4.3}$$

where

$$D(P, P_e) = \sum_{i=1}^{n_\pi} \left(p_i - \frac{1}{n_\pi} \right)^2, \tag{4.4}$$

is known as the disequilibrium factor and is defined as a distance (Euclidean or 2-norm distance) between a probability distribution P and the equiprobable distribution P_e, with $P_e = \{1/n_\pi\}_{i=1,2,\cdots,n_\pi}$. Disequilibrium gives us a way to measure how "separate" the probability distribution of the system under treatment is from the uniform distribution, the latter representing the state of maximum uncertainty [29, 30].

Complexity is minimal ($C_{LMC} = 0$) in two extreme cases: 1) Totally ordered system ($p_i = 1$ for one state and 0 for the others, $H = 0$), and 2) totally disordered system (uniform distribution, implies $p_i = 1/n_\pi$, $D = 0$). Therefore, statistical complexity takes on intermediate values for systems with a balance between order and disorder. Due to its intuitive interpretation and applicability, this approach has been used and extended in various contexts, e.g., ecological [39], economic [40], and biological systems [41].

4.3. Jensen-Shannon statistical complexity

The Jensen-Shannon statistical complexity (JSC) [31, 32] is based on the pioneering statistical complexity of López-Ruiz et al. The fundamental difference between these two quantities lies in the way distances are measured in the probability space. The JSC is defined as the product of the Shannon permutation entropy and the Jensen-Shannon divergence between the ordinal distribution $P = \{p_i(\Pi_i)\}_{i=1,2,\cdots,n_\pi}$ and the uniform distribution $P_e = \{1/n_\pi\}_{i=1,2,\cdots,n_\pi}$ instead of the Euclidean distance. We also consider the normalized version of the JSC.

$$C_{JS} = \frac{H(P) \cdot D_{JS}(P, P_e)}{D^{\max}}, \tag{4.5}$$

where

$$D_{JS}(P, P_e) = S\left[\frac{1}{2}(P + P_e)\right] - \frac{1}{2}S(P) - \frac{1}{2}S(P_e), \tag{4.6}$$

is the Jensen-Shannon divergence and

$$D^{\max} = -\frac{1}{2}\left[\frac{n_\pi! + 1}{n_\pi!}\log(n_\pi! + 1) - 2\log(2n_\pi!) + \log(n_\pi!)\right], \tag{4.7}$$

is a normalization constant; it represents the maximum possible value that $D_{JS}(P, P_e)$ can attain, occurring when $P = P_\delta$ with respect to the equiprobable distribution. Here, $P_\delta = \{\delta_{1,i}\}_{i=1,\ldots,n_\pi}$, where $\delta_{ij} = \begin{cases} 1 & \text{if } i = j \\ 0 & \text{if } i \neq j \end{cases}$ is the Kronecker delta function. P_δ represents a fully ordered distribution, whereas P_e corresponds to a completely disordered one. [32].

4.4. Tsallis permutation entropy

Tsallis entropy [33] constitutes one of the generalizations of Shannon entropy and is defined as follows:

$$S_q(P) = \frac{1}{q-1}\sum_{i=1}^{n_\pi}\left(p_i(\Pi_i) - p_i(\Pi_i)^q\right), \tag{4.8}$$

where q is a real parameter; in the limit $q \to 1$, the standard Shannon entropy (4.1) is recovered. The normalized Tsallis entropy is also obtained by dividing by the maximum entropy, namely, the entropy of the uniform distribution:

$$H_q(P) = \frac{S_q(P)}{S_q^{\max}} = (q-1)\frac{S_q(P)}{1 - (n_\pi)^{1-q}}, \tag{4.9}$$

where $S_q^{\max} = \dfrac{1 - (n_\pi)^{1-q}}{q-1}$ [33, 42].

5. Some dynamical results

The classical limit of the system addressed in this work was previously analyzed using dynamical tools in [26]. We include an illustrative figure consistent with those presented in that reference to visualize the present problem. In [26], three regions are identified in the process, as shown in Figure 1. In Figure 1, we plot the Poincaré sections for the conservative regime corresponding to: (a) $E_r = 1.000001$ and (b) $E_r = 1.2$, both within the semiquantum zone; (c) $E_r = 4.2$, representative of the transition zone; (d) $E_r = 104.8$, the critical point between the transition and classical regions where convergence begins; and (e) $E_r = 4 \cdot 10^4$, located in the classical zone. Finally, subfigure (f) depicts the Poincaré section of the conservative classical analogue. To visualize the dissipative regime (3D dissipative Poincaré sections and their respective projections) and other details, see [26].

It is important to observe in this figure the difficulty of precisely defining the boundaries between zones using Poincaré sections. The number of zones may differ from three. As mentioned in the Introduction, additional features not previously observed may also emerge. This ambiguity arises from the highly regular nature of the system's dynamics. However, the information quantifiers employed in this work will provide clarity to the problem.

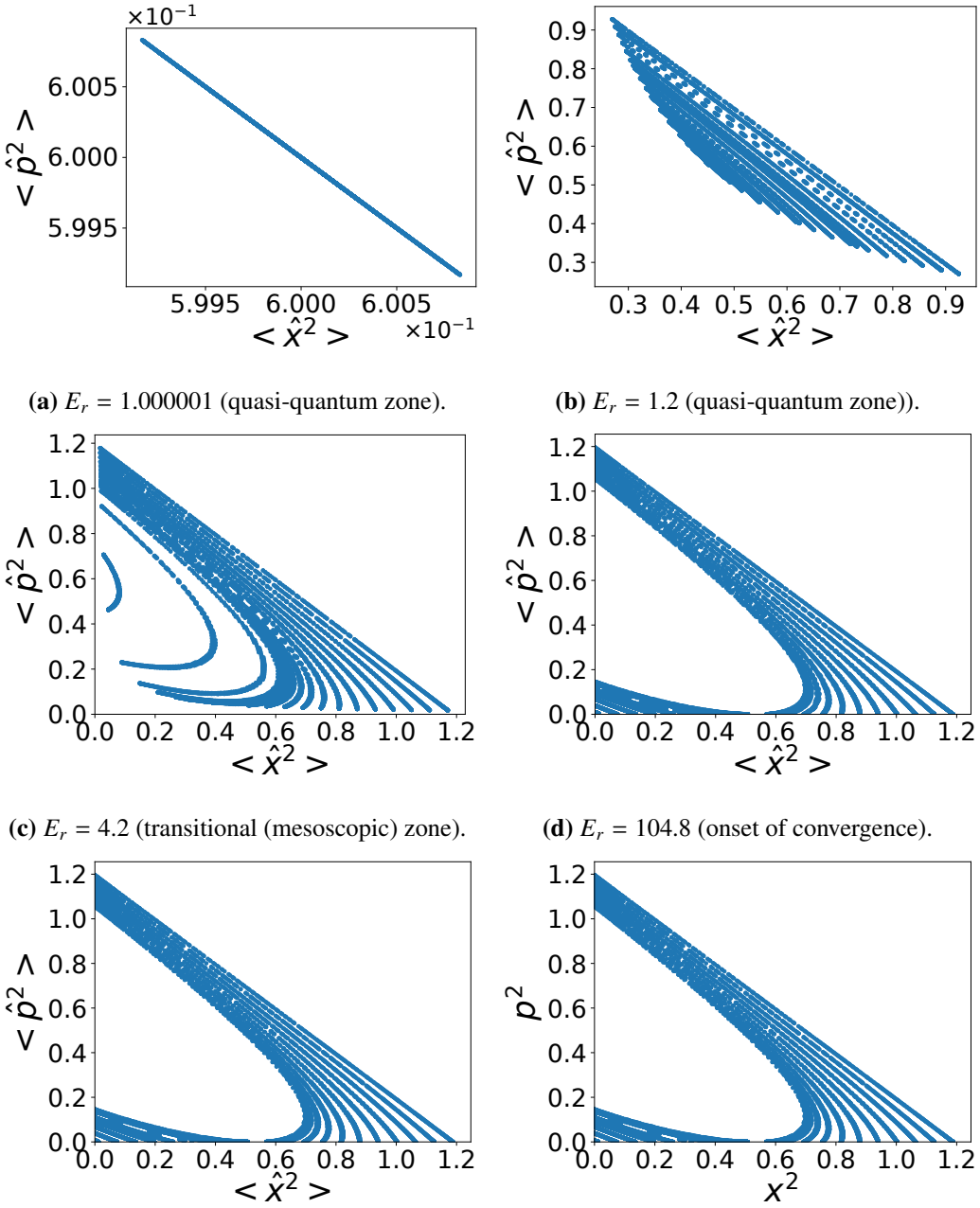

(a) $E_r = 1.000001$ (quasi-quantum zone).

(b) $E_r = 1.2$ (quasi-quantum zone)).

(c) $E_r = 4.2$ (transitional (mesoscopic) zone).

(d) $E_r = 104.8$ (onset of convergence).

(e) $E_r = 4 \cdot 10^4$ (classical zone).

(f) $E_r = \infty$ (classical analogue).

Figure 1. Poincaré sections for the conservative dynamics in the $\langle \hat{x}^2 \rangle$ vs $\langle \hat{p}^2 \rangle$ space.

6. Results

To solve Eqs (2.2) and (2.4), we adopt the parameter values $\omega_q = \omega_{cl} = e_q^{cl} = 1$. The initial conditions are $\langle \hat{L} \rangle(0) = L(0) = A(0) = 0$.

In the conservative case ($\eta = 0$), we choose $E = 0.6$. In the dissipative regime, we consider the same initial energy value $E(0) = 0.6$, with $\eta = 0.05$. In both scenarios, this value is determined by taking the limit $I \to 0$ ($E_r \to \infty$) in Eq (2.6).

We select $\langle\hat{x}^2\rangle(0) = E/\omega_q - 0.98\sqrt{(E/\omega_q)^2 - I_L}$, where $I_L = I + \langle\hat{L}\rangle(0)^2/4$. For the classical case, we set $x^2(0) = 0.02E/\omega_q$, which results from taking $I = 0$ in the same expression. From Eq (2.5), we also have $\langle\hat{p}^2\rangle(0) = I/\langle\hat{x}^2\rangle(0)$, while $p^2(0) = 0$ in the classical case.

In addition, from Eq (2.1), we deduce the value of $P_A(0)$ as follows:

$$P_A = \frac{\pm}{\omega_{cl}^{1/2}}\sqrt{2E - \omega_q\left(\langle\hat{p}^2\rangle + \langle\hat{x}^2\rangle\right) - e_q^{cl}A^2\langle\hat{x}^2\rangle - \omega_{cl}A^2}, \tag{6.1}$$

where all quantities are evaluated at the initial time. An equivalent expression to Eq (6.1) holds for the classical analogue of the system.

For the numerical computation of the information quantifiers, we employed the ordpy Python package developed by Arthur A. B. Pessa and Haroldo V. Ribeiro [38]. This open-source, computationally lightweight tool is based on the Bandt–Pompe method. It is primarily designed for analyzing time series and two-dimensional data in which the ordinal structure of the elements carries more significance than their amplitudes. The ordpy package has been widely cited across diverse fields—including physics, neuroscience, biomedical engineering, computer science, economics, and ecology—highlighting its versatility and scientific impact. According to Google Scholar, it has received more than 70 citations to date.

It should be emphasized that, due to the computational demands involved, the numerical precision achieved—both in resolving the model's temporal evolution and in computing the corresponding quantifiers—reaches the remarkable order of magnitude of 10^{-40} in each case.

We employed values of $d = 3, 4, \ldots, 7$ for the embedding dimension and $\tau = 1, 2, \ldots, 5$ for the embedding delay.

The time series corresponding to the semiclassical case were constructed using the values of $\langle\hat{x}^2\rangle(t)$, each associated with a distinct value of E_r (or I). In the classical case ($I = 0$), we considered the single series composed of the $x^2(t)$ values. In both scenarios, we took $N = 20000$ points per series. The condition $N \gg d!$ is satisfied for all values of d [27].

We present the results through graphical representations that illustrate the dependence of various quantifiers on the relative energy E_r. The values of E_r were sampled with a uniform step size of $\Delta E_r = 0.2$. While the figures shown here correspond exclusively to this sampling resolution, we verified that simulations performed with finer steps—$\Delta E_r = 0.1$, 10^{-2}, and 10^{-3}—yield consistent results. These supplementary computations confirm that the local features of the quantifiers remain unchanged. This robustness with respect to resolution supports the validity of our findings and justifies the use of the coarser grid in the present analysis.

In all figures, we observe low values of the information quantifiers, in contrast to those obtained for the chaotic Hamiltonian described in [27]. This behavior is consistent with the regularity observed in the Poincaré sections [26].

6.1. Analysis and findings on Shannon-based quantifiers

The analysis begins with a detailed examination of the Shannon entropy H (4.2) and the statistical complexities C_{LMC} (4.3) and C_{JS} (4.5), considering $d = 5$ and $\tau = 1$ as representative parameters. The corresponding outcomes are shown in Figures 2, 3, and 5. Results obtained with other combinations of d and τ show no significant differences, as will be discussed later. The study then proceeds with the application of quantifiers derived from generalized statistical frameworks.

In Figure 2, we plot the semiclassical normalized entropy H versus the relative energy E_r for both the conservative and dissipative regimes. Each regime exhibits two distinct regions, characterized by differing fluctuation levels. In both cases, a critical point is identified—at $E_r \approx 104.8$ for the conservative regime and at $E_r \approx 123.0$ for the dissipative one. Around these points, H transitions from a region of monotonic growth to a nearly flat segment, suggesting the onset of classical behavior. These critical points thus serve as natural candidates for defining thresholds in the entropy landscape. Beyond them, H converges to the classical entropy values: $H_c^{cl} = 0.1768$ and $H_d^{cl} = 0.17207$, respectively.

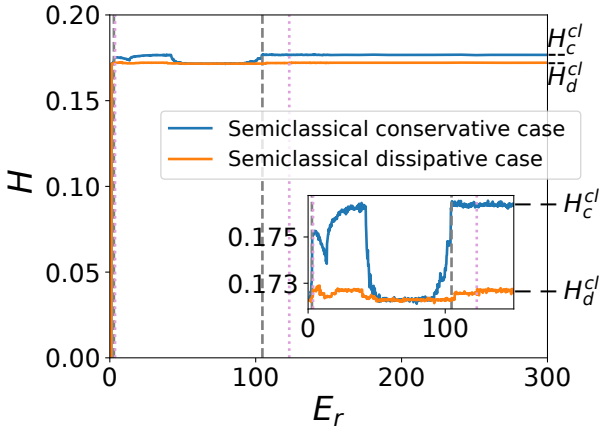

Figure 2. Permutation entropy H vs. E_r for conservative (blue) and dissipative (orange) regimes. In the conservative case, the quasi-quantum region spans $E_r > 1$ to ≈ 2.8, followed by a transition zone up to ≈ 104.8, beyond which H converges to its classical analogue value H_c^{cl}. In the dissipative regime, these intervals shift to $E_r > 1$ to ≈ 3.6 and ≈ 3.6 to ≈ 123.0, where convergence begins toward H_d^{cl}. Gray dashed lines mark conservative boundaries; plum lines indicate dissipative transitions. Inset: magnified view of the transition region.

Specifically, a comparison of the increments in H as a function of E_r reveals a pronounced asymmetry around these critical points. For the conservative system, the difference ΔH between the critical point and the immediately subsequent value is on the order of $5 \cdot 10^{-5}$, decreasing progressively and stabilizing near 10^{-6} as E_r increases. In contrast, the variation of H between the preceding point and the critical value reaches approximately $5 \cdot 10^{-4}$, with a tendency to grow as one moves further backward. This asymmetry provides a quantitative basis for identifying a natural threshold that marks the onset of the region referred to as the classical zone.

In this region, the fluctuations $\Delta H = H_{\max} - H_{\min}$ remain below 10^{-6}, in contrast to variations on the order of $\Delta H = 5 \cdot 10^{-3}$ observed throughout the figure. Similar results are found in the dissipative case and across all quantifiers. To reinforce this interpretation, we will complete the threshold analysis using numerical derivatives of H concerning E_r later on, when we examine the other threshold of the process, allowing for a more precise characterization of the transition.

The analysis of the Poincaré sections presented in [26] revealed two distinguishable regions within the fluctuating zone mentioned above, with boundaries that are difficult to pinpoint: a quasi-quantum zone and a transition zone. These regions, illustrated in Figure 1, are consistently observed in both the conservative and dissipative regimes.

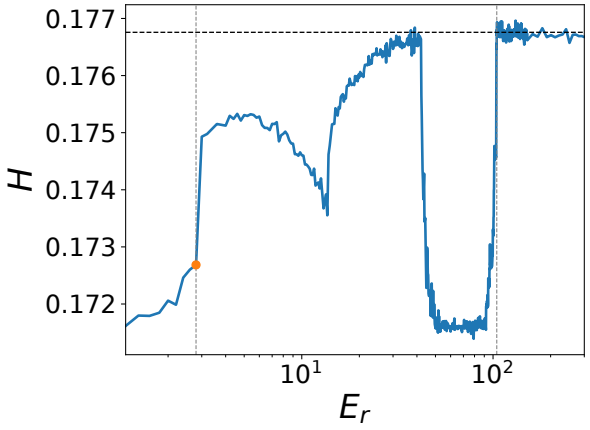

Figure 3. Permutation entropy H as a function of the relative energy E_r in the conservative system. The horizontal axis is plotted on a logarithmic scale. The orange data point indicates $E_r \approx 2.8$, where the entropy shows its first abrupt change.

Figure 3 shows H as a function of E_r for the conservative system. The plot reveals the first abrupt change in entropy at the critical point $E_r \approx 2.8$ (associated with the orange marker). The entropy variations ΔH between the H-value at this critical point and its preceding (and neighboring) points remain below 10^{-5}—a difference greater than those near the classical limit but smaller than the maximum observed across the dataset. In contrast, the variation immediately following the marker exceeds this value. Specifically, the entropy variation before the critical point remains below 10^{-5}, while the variation with the next data point reaches approximately 10^{-3}. The comparison of finite differences around a point is widely employed in statistical physics and quantum dynamics to detect singularities or, as in the present work, transitions [43, 44].

Figure 4a displays the numerical derivative of the entropy H with respect to E_r, dH/dE_r, versus E_r. The analysis reveals two prominent peaks at the previously identified critical points: one at $E_r \approx 2.8$ and another at $E_r \approx 104.8$, with amplitudes of $dH/dE_r \approx 0.00582$ and ≈ 0.00499, respectively. These values exceed those of the remaining local maxima, indicating abrupt changes in the entropy slope. Additional, smaller peaks correspond to intermediate variations within the transition zone. A third notable maximum appears at the sharp drop of H, marking the onset of an almost flat region of highly regular dynamics that culminates at the peak near $E_r \approx 104.8$ (see Figure 3).

Figure 4b presents the second numerical derivative of the entropy H with respect to the relative energy E_r, i.e., d^2H/dE_r^2 as a function of E_r. Inflection points are observed at $E_r \approx 2.8$, marking the onset of the transition region, and at $E_r \approx 104.8$, associated with the classical zone. The presence of these curvature changes, accompanied by large variations in their vicinity, reflects abrupt shifts in the acceleration of entropy, reinforcing the delineation of distinct dynamics within the system. Additionally, several other inflection points appear in the intermediate region, coinciding with the positions of the secondary peaks in dH/dE_r. In the case of the third peak, it suggests that the relative variation of H stabilizes, entering a zone of regular dynamics.

As previously mentioned, although the figures were plotted using a step size of $\Delta E_r = 0.2$, we verified that simulations performed with finer steps yield consistent results. In particular, an adaptive refinement with local steps of $\Delta E_r = 10^{-3}$ was applied near suspected transition zones. For this reason,

the position of each critical point is determined with a maximum error of $\Delta E_r = \pm 5 \cdot 10^{-4}$. This accuracy holds for all information-theoretic quantifiers analyzed. These studies confirm that the critical points mentioned are indeed thresholds.

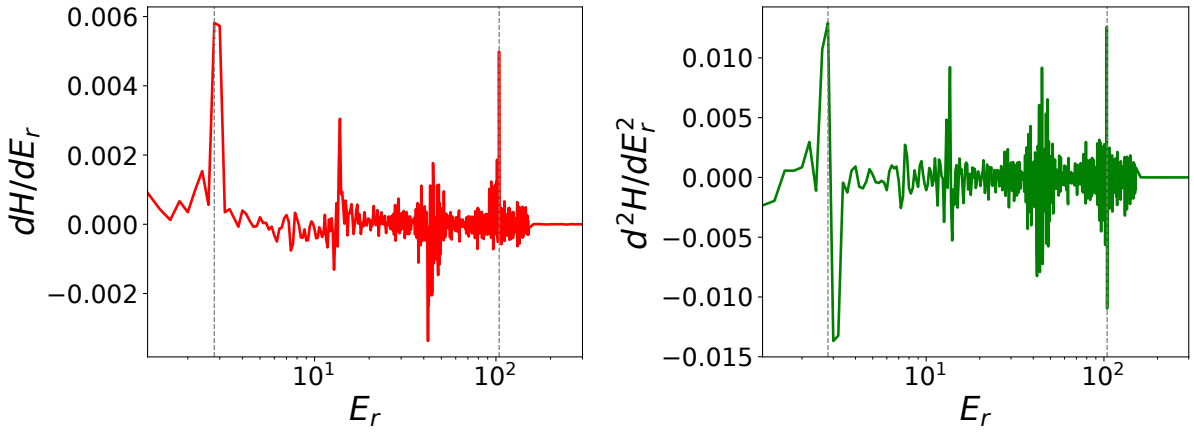

(a) **(b)**

Figure 4. (a) First numerical derivative of the entropy H with respect to E_r. (b) Second numerical derivative of H with respect to E_r. In both plots, the vertical gray lines indicate $E_r \approx 2.8$ (onset of the transition zone) and $E_r \approx 104.8$ (onset of the classical convergence zone), respectively. These correspond to the conservative system shown in Figure 3.

In summary, as illustrated in Figure 2, the conservative regime exhibits a quasi-quantum zone for $E_r > 1$ up to the threshold at $E_r \approx 2.8$, followed by a transition region extending to the threshold at $E_r \approx 104.8$, beyond which the system enters the classical zone. In the dissipative case (orange curve), these zones shift: the quasi-quantum region spans up to $E_r \approx 3.6$, and the transition zone reaches $E_r \approx 123.0$, threshold of the classical zone. The transition region can be associated with a mesoscopic one because of the significant presence of quantum features. The inset provides a more detailed view of the curve shapes within this region. The zone of convergence to the fully classical system must correspond to a decoherence process [26]. This behavior holds for all information-theoretic quantifiers considered in this work.

Figures 5a and 5b display the statistical complexity measures C_{JS} and C_{LMC} as functions of E_r. In both cases, the zones emerge within the same E_r ranges for the conservative (blue curve) and dissipative (orange curve) regimes, matching those identified through the corresponding entropy measures. This consistent alignment of zone boundaries and associated criteria across entropy and complexity analyses reinforces the robustness of the classification and suggests a coherent underlying structure governing both descriptions. Each plot includes a magnified inset of the transition zone. The corresponding classical analogue values to which the complexities converge are: $C_c^{cl} = 0.16401$ and $C_d^{cl} = 0.16058$ for C_{JS}; and $C_c^{cl} = 0.13533$ and $C_d^{cl} = 0.13426$ for C_{LMC}.

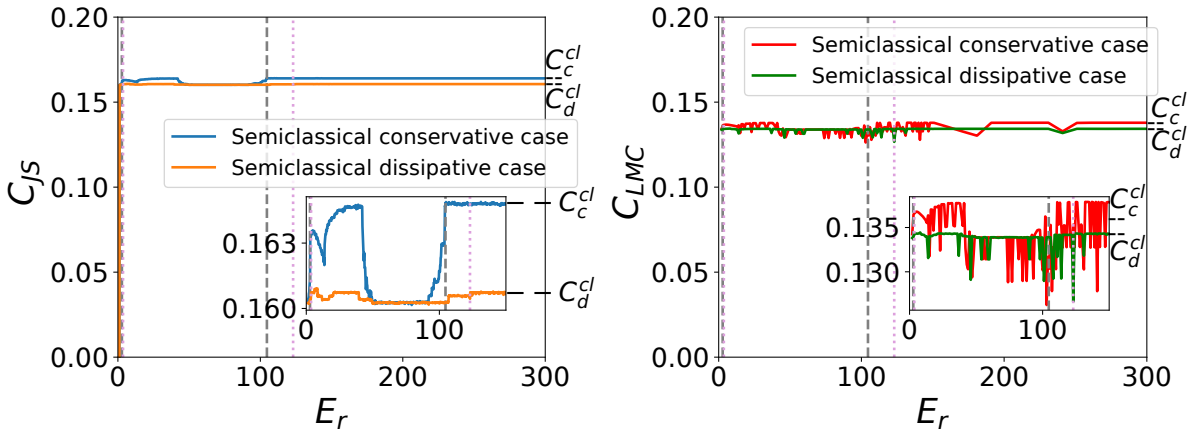

(a) **(b)**

Figure 5. Statistical complexity vs. E_r. Vertical lines mark quasi-quantum, transitional, and classical zones—gray dashed for conservative and plum dotted for dissipative dynamics—matching entropy-based E_r ranges from Figure 2. Insets focus on transition regions.

We note that the representative plots of H and C_{JS} (4.5) clearly exhibit similar qualitative behavior, albeit at different scales. This pattern arises because the disequilibrium factor (4.6) remains nearly constant around its average value—$D_{JS} \approx 0.92985$ for the conservative regime and $D_{JS} \approx 0.93337$ for the dissipative one—across all values of E_r.

The corresponding disequilibrium factor (4.4) for the C_{LMC} (4.3) complexities exhibits larger fluctuations around its average values: $D_{LMC\,c} \approx 0.76944$ and $D_{LMC\,d} \approx 0.77906$, corresponding to the conservative and dissipative dynamics, respectively. These fluctuations result in a less smooth behavior of the C_{LMC} curve compared to the C_{JS} one, a phenomenon observed in both regimes. Additionally, the different normalization criteria used in the definitions of C_{LMC} and C_{JS} lead to a variation in scale. To enable a meaningful comparison, the C_{LMC} complexity curve was rescaled by multiplying all its values by the factor 1.196, thus matching the mean values of C_{LMC} and C_{JS}. After applying this rescaling, it was observed that, despite the pronounced amplitude fluctuations of C_{LMC} relative to C_{JS}, both curves share a similar overall profile; in other words, C_{LMC} fluctuates approximately around C_{JS}. This behavior confirms the structural coherence of the underlying dynamic pattern. The scale factor of 1.196 derives from the relation between the disequilibrium factors involved in each complexity formulation.

On the other hand, aside from minor fluctuations, both the quantifiers and their range between maximum and minimum bounds are slightly higher in the conservative regime than in the dissipative one. Although convergence to the fully classical system (2.4) begins somewhat earlier in the conservative regime, the associated transition zone extends over a broader range of E_r in the dissipative regime. This behavior can be interpreted as a smoothening effect, consistent with the previously described characteristics.

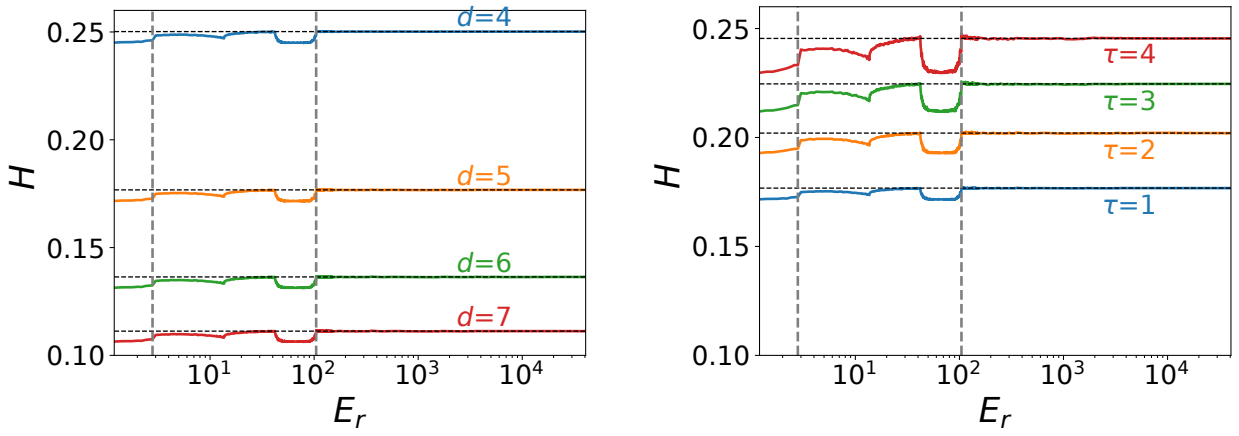

(a) **(b)**

Figure 6. H as a function of E_r in the conservative system. The horizontal axis is plotted on a logarithmic scale. (a) Results for embedding dimensions $d = 4$ to 7, with fixed delay $\tau = 1$. (b) Results for embedding delays $\tau = 1$ to 4, with fixed dimension $d = 5$. In both cases, the three range zones of the process remain unchanged. The overall shape of the curves is preserved, except for a rescaling effect. The transitional zone lies between the vertical dashed lines, while the horizontal ones mark the entropy of the classical system.

Figure 6 shows the Shannon permutation entropy as a function of the relative energy E_r in the conservative system. To highlight variations at low energy levels, the horizontal axis is displayed on a logarithmic scale, where the process zones become more clearly distinguishable. Figure 6a corresponds to embedding dimensions from $d = 4$ to $d = 7$ (in steps of one), with a fixed embedding delay $\tau = 1$. Conversely, Figure 6b explores delay values from $\tau = 1$ to 4 (also in steps of one), while keeping the embedding dimension fixed at $d = 5$. In both cases, the three range zones of the process remain unchanged; the overall shape of the curves is also preserved, except for a rescaling effect governed by normalization factors dependent on d and τ. The transitional zone lies between the vertical gray dashed lines. The horizontal black dashed lines indicate the Shannon permutation entropy of the fully classical system, which also depends on d and τ. In all cases, the semiclassical regime tends to converge toward the corresponding classical one.

6.2. Analysis and findings on Tsallis-based quantifiers

A comparison with alternative information-theoretic quantifiers proves useful for gauging the robustness of the findings.

The analyses based on the Tsallis quantifiers show complete agreement with the results obtained using the Shannon-based measures. The zones along the path to the classical limit are precisely the same in both cases.

In this section, all figures present results for $d = 5$ and $\tau = 1$, although the outcomes obtained with the other parameters introduced earlier are qualitatively similar.

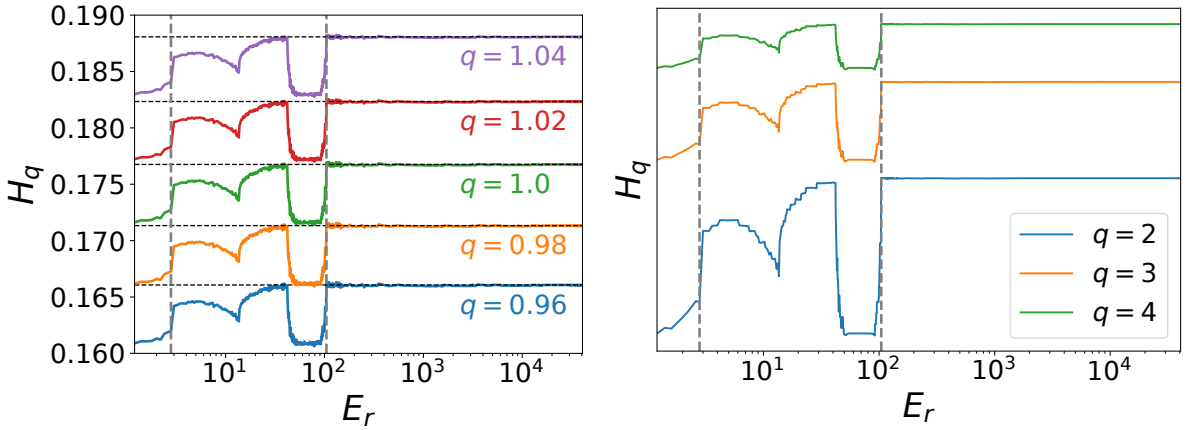

(a) **(b)**

Figure 7. Tsallis permutation entropy in the conservative regime as a function of E_r for various q values, with $d = 5$ and $\tau = 1$. Horizontal dashed lines indicate the classical entropy for each q, while vertical dashed lines mark the region boundaries obtained in the Shannon case. (a) Small q values, where increasing q primarily shifts the curves upward. (b) Larger q values, showing more pronounced shape changes in the quasi-quantum and transitional regions. For clarity, curves are vertically offset and the vertical axis scale is omitted.

Figure 7 presents the conservative regime of Tsallis entropy for different values of the entropic index q. The horizontal axis is shown on a logarithmic scale to enhance the resolution of the curves at low E_r values. The entropy H_q exhibits a vertical shift and a change in shape, both dependent on the parameter q. Subfigure 7a considers small values of q, allowing us to observe that as q increases, the curve shifts vertically upward ($H_{q=0.95,\max} < \cdots < H_{q=1.04,\max}$), while the maximum variation ΔH_q across the entire series for each corresponding q value decreases. The shape change is barely noticeable.

Figure 7b shows the behavior of H_q as a function of E_r, considering large values of q, which allow us to observe a shape change in the regions referred to as quasi-quantum and transitional. This behavior is a direct consequence of the properties of Tsallis entropy. To facilitate comparison, the curves have been vertically shifted, and the vertical axis scale is therefore omitted.

A particularly relevant result is that the position of the transition points (identified and discussed in the previous subsection) remains constant for all studied values of q, suggesting that the system's dynamics are independent of the nonextensivity parameter and reinforcing the results obtained using Shannon entropy.

7. Conclusions

In this work, the conservative and dissipative dynamics governed by the semiclassical Hamiltonian (2.1), which combines quantum and classical components, were investigated. Particular attention was devoted to the classical limit, interpreted as the convergence toward the behavior described by its classical analogue (2.3), where all variables are purely classical. This transition was explored as a function of the relative energy E_r (2.6), intrinsically connected to the uncertainty principle, with the asymptotic regime defined by $E_r \to \infty$.

To characterize this process, information-theoretic quantifiers were employed. The first approach relied on Shannon entropy, H (4.2), complemented by two complexity measures: the pioneering formulation introduced by López-Ruiz et al. [28–30], C_{LMC} (4.3), and the JSC [31, 32], C_{JS} (4.5). To confirm the consistency of the results, a second framework was adopted based on a q-generalized perspective, employing Tsallis entropy, H_q (4.9). This alternative formulation yielded results that aligned with those obtained from the Shannon-based analysis, thereby reinforcing the robustness of the conclusions across distinct entropic paradigms [32, 38].

The probability distribution used to evaluate all these quantities was extracted from the time series using the Bandt and Pompe permutation method [34], a methodology that has proven to be both robust and reliable. We employed embedding dimensions ranging from $d = 4$ to 7, and delays from $\tau = 1$ to 4. In [26], the same problem was previously addressed using dynamical tools, including Poincaré sections and three-dimensional projections. That study identified three distinct zones: a quasi-quantum region, a transitional mesoscopic domain, and a classical zone, which exhibits convergence toward the behavior of the classical analogue. However, due to the regular nature of the system dynamics, the boundaries between these zones were blurred (see Figure 1). Moreover, no adequate quantitative analyses were performed.

This regularity is also apparent in the figures of the present work, as evidenced by the consistently low values of all information-theoretic quantifiers. Moreover, the respective values exhibit a very narrow variation band throughout the domain. In general, aside from minor fluctuations, both the quantifiers and their range between maximum and minimum bounds are higher in the conservative regime than in the dissipative one.

All figures from 2 to 7 consistently exhibit the same structural zones that define the trajectory toward the classical limit. We confirmed the presence of the zones associated with the convergence process to the fully classical system, as described in [26]. We also identified the boundaries between regions with improved precision. These zones fall within the same range of E_r for all quantifiers analyzed. This applies to both Shannon and Tsallis statistics.

A first indication of zone transitions arises from the presence of prominent peaks and plateaus in the entropy curves themselves. These features mark shifts in the system's informational structure and coincide with the expected boundaries between zones. To refine these observations, we performed a quantitative analysis of the transition thresholds by evaluating the first and second derivatives of the entropic measures with respect to E_r. This approach allowed us to detect inflection points and local extrema that confirm and sharpen the zone delimitations. The thresholds obtained are consistent across quantifiers and exhibit minimal dispersion, providing a rigorous basis for the segmentation and complementing the qualitative observations reported in [26].

In the conservative scenario, the quasi-quantum region extends from $E_r > 1$ to approximately $E_r = 2.8$. The mesoscopic transition zone follows, covering the range from $E_r \approx 2.8$ to $E_r \approx 104.8$. Beyond this point, the system enters the convergence domain as it approaches its classical quantifier analogue value. For the dissipative regime, the quasi-quantum region extends from $E_r > 1$ to $E_r \approx 3.6$, and the transition zone continues up to $E_r \approx 123.0$. Beyond this threshold, the system enters a convergence-dominated domain, approaching its corresponding classical quantifier analogue value.

The figures of H and C_{JS} exhibit similar profiles, albeit differing in scale. This behavior stems from the fact that the disequilibrium factor D_{JS} remains nearly constant across all values of E_r in both the conservative and dissipative scenarios. In the case of C_{LMC} complexity, the disequilibrium factor D

is likewise quasi-constant, though it displays more pronounced fluctuations around its mean value in both regimes. Despite these amplitude variations and the scale difference relative to C_{JS}, C_{LMC} retains a comparable overall shape.

In summary, this study has fulfilled its primary objective of characterizing the underlying process using information-theoretic quantifiers, unveiling features that remain inaccessible through purely dynamical approaches. In addition, the observed structural pattern is consistent with previous findings for semiclassical Hamiltonians with markedly different dynamics. This consistency supports the idea of a possible generalization with potential implications for both semiclassical and quantum theories.

Author contributions

Gaspar Gonzalez Acosta: Conceptualization, Methodology, Software, Formal analysis, Investigation, Writing-original draft; Andrés M. Kowalski: Conceptualization, Methodology, Formal analysis, Investigation, Writing-original draft, Supervision.

Use of AI tools declaration

The authors declare that they have not used Artificial Intelligence (AI) tools in the creation of this article.

Conflict of interest

The authors declare that they have no conflicts of interest.

References

1. W. Struyve, Semi-classical approximations based on bohmian mechanics, *Int. J. Mod. Phys. A*, **35** (2020), 2050070. https://doi.org/10.1142/S0217751X20500700
2. V. Allori, N. Zanghì, On the classical limit of quantum mechanics, *Found. Phys.*, **39** (2009), 20–32. https://doi.org/10.1007/s10701-008-9259-4
3. G. Hooft, Physics on the boundary between classical and quantum mechanics, *J. Phys.: Conf. Ser.*, **504** (2014), 012003. https://doi.org/10.1088/1742-6596/504/1/012003
4. D. Dieks, A. Lubberdink, How classical particles emerge from the quantum world, *Found. Phys.*, **41** (2011), 1051–1064. https://doi.org/10.1007/s10701-010-9515-2
5. M. Ludwig, B. Kubala, F. Marquardt, The optomechanical instability in the quantum regime, *New J. Phys.*, **10** (2008), 095013. https://doi.org/10.1088/1367-2630/10/9/095013
6. J. Fink, L. Steffen, P. Studer, L. S. Bishop, M. Baur, R. Bianchetti, et al., Quantum-to-classical transition in cavity quantum electrodynamics, *Phys. Rev. Lett.*, **105** (2010), 163601. https://doi.org/10.1103/physrevlett.105.163601
7. J. Raftery, D. Sadri, S. Schmidt, H. E. Türeci, A. A. Houck, Observation of a dissipation-induced classical to quantum transition, *Phys. Rev. X*, **4** (2014), 031043. https://doi.org/10.1103/physrevx.4.031043

8. E. Joos, H. D. Zeh, C. Kiefer, D. J. Giulini, J. Kupsch, I.-O. Stamatescu, *Decoherence and the appearance of a classical world in quantum theory*, Berlin, Heidelberg: Springer, 2003. https://doi.org/10.1007/978-3-662-05328-7
9. M. P. Das, Mesoscopic systems in the quantum realm: fundamental science and applications, *Adv. Nat. Sci: Nanosci. Nanotechnol.*, **1** (2010), 043001. https://doi.org/10.1088/2043-6262/1/4/043001
10. T. Brandes, Coherent and collective quantum optical effects in mesoscopic systems, *Phys. Rep.*, **408** (2005), 315–474. https://doi.org/10.1016/j.physrep.2004.12.002
11. F. Iachello, N. Zamfir, Quantum phase transitions in mesoscopic systems, *Phys. Rev. Lett.*, **92** (2004), 212501. https://doi.org/10.1103/physrevlett.92.212501
12. F. Bloch, Nuclear induction, *Phys. Rev.*, **70** (1946), 460. https://doi.org/10.1103/physrev.70.460
13. P. W. Milonni, M. Shih, J. R. Ackerhalt, *Chaos in Laser-Matter Interactions*, World Scientific Publishing Company, 1987. https://doi.org/10.1142/0323
14. A. A. Budini, Quantum–classical hybrid dynamics: Coupling mechanisms and diffusive approximation, *Open Syst. Inf. Dyn.*, **31** (2024), 2450013. https://doi.org/10.1142/S1230161224500136
15. A. D. Bermúdez Manjarres, M. Reginatto, S. Ulbricht, Three statistical descriptions of classical systems and their extensions to hybrid quantum–classical systems, *Eur. Phys. J. Plus*, **139** (2024), 780. https://doi.org/10.1140/epjp/s13360-024-05452-0
16. T. Micklitz, A. Altland, Semiclassical theory of chaotic quantum resonances, *Phys. Rev. E*, **87** (2013), 032918. https://doi.org/10.1103/PhysRevE.87.032918
17. S. Prants, Quantum–classical correspondence in chaotic dynamics of laser-driven atoms, *Phys. Scr.*, **92** (2017), 044002. https://doi.org/10.1088/1402-4896/aa5f8f
18. R. F. Ribeiro, K. Burke, Deriving uniform semiclassical approximations for one-dimensional fermionic systems, *J. Chem. Phys.*, **148** (2018), 194103. https://doi.org/10.1063/1.5025628
19. F. Minganti, A. Miranowicz, R. W. Chhajlany, F. Nori, Quantum exceptional points of non-hermitian hamiltonians and liouvillians: The effects of quantum jumps, *Phys. Rev. A*, **100** (2019), 062131. https://doi.org/10.1103/PhysRevA.100.062131
20. M. Bastarrachea-Magnani, S. Lerma-Hernández, J. Hirsch, Comparative quantum and semiclassical analysis of atom-field systems. ii. chaos and regularity, *Phys. Rev. A*, **89** (2014), 032102. https://doi.org/10.1103/PhysRevA.89.032102
21. V. Allori, N. Zanghì, On the classical limit of quantum mechanics, *Found. Phys.*, **39** (2009), 20–32. https://doi.org/10.1007/s10701-008-9259-4
22. J. Kurchan, Quantum bound to chaos and the semiclassical limit, *J. Stat. Phys.*, **171** (2018), 965–979. https://doi.org/10.1007/s10955-018-2052-7
23. A. C. Oliveira, M. C. Nemes, K. F. Romero, Quantum time scales and the classical limit: Analytic results for some simple systems, *Phys. Rev. E*, **68** (2003), 036214. https://doi.org/10.1103/PhysRevE.68.036214
24. A. Kowalski, A. Plastino, A. Proto, Semiclassical model for quantum dissipation, *Phys. Rev. E*, **52** (1995), 165. https://doi.org/10.1103/PhysRevE.52.165

25. A. M. Kowalski, A. Plastino, A. Proto, Classical limits, *Phys. Lett. A*, **297** (2002), 162–172. https://doi.org/10.1016/S0375-9601(02)00034-8
26. G. Gonzalez Acosta, A. Plastino, A. Kowalski, Dynamical classic limit: Dissipative vs conservative systems, *Chaos*, **33** (2023), 013126. https://doi.org/10.1063/5.0126040
27. A. Kowalski, M. Martín, A. Plastino, O. Rosso, Bandt–pompe approach to the classical-quantum transition, *Phys. D*, **233** (2007), 21–31. https://doi.org/10.1016/j.physd.2007.06.015
28. R. Lopez-Ruiz, H. L. Mancini, X. Calbet, A statistical measure of complexity, *Phys. Lett. A*, **209** (1995), 321–326. https://doi.org/10.1016/0375-9601(95)00867-5
29. R. Lopez-Ruiz, Complexity in some physical systems, *Int. J. Bifurcation Chaos*, **11** (2001), 2669–2673. https://doi.org/10.1142/S0218127401003711
30. X. Calbet, R. López-Ruiz, Tendency towards maximum complexity in a nonequilibrium isolated system, *Phys. Rev. E*, **63** (2001), 066116. https://doi.org/10.1103/PhysRevE.63.066116
31. P. W. Lamberti, M. Martin, A. Plastino, O. Rosso, Intensive entropic non-triviality measure, *Phys. A*, **334** (2004), 119–131. https://doi.org/10.1016/j.physa.2003.11.005
32. M. Martin, A. Plastino, O. A. Rosso, Generalized statistical complexity measures: Geometrical and analytical properties, *Phys. A*, **369** (2006), 439–462. https://doi.org/10.1016/j.physa.2005.11.053
33. C. Tsallis, Entropic nonextensivity: A possible measure of complexity, *Chaos, Solitons & Fractals*, **13** (2002), 371–391. https://doi.org/10.1016/S0960-0779(01)00019-4
34. C. Bandt, B. Pompe, Permutation entropy: A natural complexity measure for time series, *Phys. Rev. Lett.*, **88** (2002), 174102. https://doi.org/10.1103/PhysRevLett.88.174102
35. K. Keller, M. Sinn, Ordinal analysis of time series, *Phys. A*, **356** (2005), 114–120. https://doi.org/10.1016/j.physa.2005.05.022
36. P. M. Saco, L. C. Carpi, A. Figliola, E. Serrano, O. A. Rosso, Entropy analysis of the dynamics of el niño/southern oscillation during the holocene, *Phys. A*, **389** (2010), 5022–5027. https://doi.org/10.1016/j.physa.2010.07.006
37. L. Zunino, M. C. Soriano, I. Fischer, O. A. Rosso, C. R. Mirasso, Permutation-information-theory approach to unveil delay dynamics from time-series analysis, *Phys. Rev. E*, **82** (2010), 046212. https://doi.org/10.1103/PhysRevE.82.046212
38. A. A. Pessa, H. V. Ribeiro, ordpy: A python package for data analysis with permutation entropy and ordinal network methods, *Chaos*, **31**, https://doi.org/10.1063/5.0049901
39. J. R. C. Piqueira, S. H. V. de Mattos, Note on lmc complexity measure, *Ecol. Modell.*, **222** (2011), 3603–3604. https://doi.org/10.1016/j.ecolmodel.2011.08.012
40. J. R. C. Piqueira, S. H. V. L. d. Mattos, Lmc and sdl complexity measures: A tool to explore time series, *Complexity*, **2019** (2019), 2095063. https://doi.org/10.1155/2019/2095063
41. R. E. Monge, J. L. Crespo, Analysis of data complexity in human dna for gene-containing zone prediction, *Entropy*, **17** (2015), 1673–1689. https://doi.org/10.3390/e17041673
42. L. Zunino, D. Pérez, A. Kowalski, M. Martín, M. Garavaglia, A. Plastino, et al., Fractional brownian motion, fractional gaussian noise, and tsallis permutation entropy, *Phys. A*, **387** (2008), 6057–6068. https://doi.org/10.1016/j.physa.2008.07.004

43. L. Zdeborová, F. Krzakala, Statistical physics of inference: Thresholds and algorithms, *Adv. Phys.*, **65** (2016), 453–552. https://doi.org/10.1080/00018732.2016.1211393

44. A. Zvyagin, Dynamical quantum phase transitions, *Low Temp. Phys.*, **42** (2016), 971–994. https://doi.org/10.1063/1.4969869

45. F. Cooper, J. Dawson, S. Habib, R. D. Ryne, Chaos in time-dependent variational approximations to quantum dynamics, *Phys. Rev. E*, **57** (1998), 1489. https://doi.org/10.1103/PhysRevE.57.1489

46. Y. Alhassid, R. Levine, Connection between the maximal entropy and the scattering theoretic analyses of collision processes, *Phys. Rev. A*, **18** (1978), 89. https://doi.org/10.1103/PhysRevA.18.89

47. R. Levine, D. Napoli, D. Otero, A. Plastino, A. Proto, Maximum entropy approach to nuclear fission processes, *Nucl. Phys. A*, **454** (1986), 338–358. https://doi.org/10.1016/0375-9474(86)90272-1

48. V. I. Arnold, *Mathematical Methods of Classical Mechanics*, 2 Eds., New York: Springer, 2013. https://doi.org/10.1007/978-1-4757-2063-1

49. S. Boyd, L. Vandenberghe, *Convex Optimization*, Cambridge: Cambridge University Press, 2004. https://doi.org/10.1017/CBO9780511804441

50. W. Rudin, *Functional Analysis*, 2 Eds., McGraw-Hill, 1991.

Appendix A. Semiclassical model

Our semiclassical Hamiltonian is (2.1). In our methodology, the time evolution of all operators is the canonical one. The Hamiltonian also depends on the classical variables A and P_A, which represent the reservoir. These classical quantities obey Hamilton's equations, of course, where the temporal generator is the mean value of the Hamiltonian [25,45]. If we add to the system an appropriate ad hoc term, we get dissipation [24].

Thus, for a given operator, we have

$$\frac{d\hat{O}}{dt} = \frac{i}{\hbar}\left[\hat{H}, \hat{O}\right]. \tag{A1}$$

The evolution of $\langle\hat{O}\rangle \equiv \mathrm{Tr}\left[\rho\hat{O}\,(t)\right]$ is provided by

$$\frac{d\langle\hat{O}\rangle}{dt} = \frac{i}{\hbar}\left\langle\left[\hat{H}, \hat{O}\right]\right\rangle, \tag{A2}$$

using a suitable density operator $\rho\,(0)$.

$[\,\hat{H}, \hat{O}_i\,]$ can always be cast as [46,47]

$$[\,\hat{H}, \hat{O}_i\,] = i\hbar\sum_{j=1}^{q} g_{ji}\hat{O}_j\,, \qquad i = 0, 1, \ldots, q, \tag{A3}$$

where we can have $q \to \infty$. We are interested in finite q-values. In this case, it is said that the set of operators $\hat{O}_i$, $i = 0, 1, \ldots, q$, closes a Lie semi-algebra with $\hat{H}$ [46,47].

For a semiclassical Hamiltonian like (2.1), the coefficients g_{ji} depend on the classical variables A and P_A. As previously mentioned, these variables evolve according to Hamilton's equations, with the expectation value $\langle \hat{H} \rangle$ acting as the generator of time evolution:

$$\frac{dA}{dt} = \frac{\partial \langle \hat{H} \rangle}{\partial P_A}, \tag{A4a}$$

$$\frac{dP_A}{dt} = -\frac{\partial \langle \hat{H} \rangle}{\partial A} - \eta P_A. \tag{A4b}$$

In the case of finite q, Eqs (A2) and (A4) form a first-order autonomous system of coupled differential equations (ODEs). If $\eta > 0$, the system is dissipative; if $\eta = 0$, it is conservative.

To analyze this behavior [24], it is convenient to define a vector $\vec{v}(t)$ that includes both quantum and classical variables: the mean values of the operators $\hat{O}_i$ for $i = 0, 1, \ldots, q$, appearing in Eqs (A2), along with the classical variables A and P_A. The system defined by Eqs (A2) and (A4) can then be rewritten as [24]:

$$\frac{d\vec{v}}{dt} = \vec{F}(\vec{v}). \tag{A5}$$

The vector $\vec{v}(t)$ evolves in a $(q + 2)$-dimensional space, hereafter referred to as "v-space." We consider volume elements V_S within this space, bounded by a surface S, both defined in a generalized sense. The dissipative term η induces a contraction of V_S [48]. The divergence of our vector is seen to be $-\eta$, given the fact that the matrix G in Eqs (A3) is traceless. This happens because of the canonical character of Eqs (A1). Consequently. we must have [24]

$$\frac{dV_S(t)}{dt} = -\eta V_S(t). \tag{A6}$$

Accordingly, we deal with a dissipative system [48]. If the classical Hamiltonian is of the form

$$H_{cl} = \frac{1}{2M} P_A^2 + V(A), \tag{A7}$$

then the time-evolution of the total energy $\langle \hat{H} \rangle$ becomes

$$\frac{d\langle \hat{H} \rangle}{dt} = -\frac{\eta}{M} P_A^2. \tag{A8}$$

Its meaning is to be ascertained through the lens of Eq (A6) [24].

This methodology enables a dynamical description in which no quantum rules of the subquantum system are violated, for instance, the commutation relations are trivially conserved at all times, since the quantum evolution is the canonical one for an effective time-dependent Hamiltonian (A and P_A-play the role of time-dependent parameters of the quantum system). This occurs in both dissipative and conservative cases [26].

Appendix B. Demonstrations of the inequality $I \geq \hbar^2/4$

We start from the Schrödinger-Robertson uncertainty relation.

$$I_\Delta = \Delta^2 x \; \Delta^2 p - \frac{\Delta L^2}{4} \geq \hbar^2/4 \tag{B1}$$

where

$$\Delta^2 x = \langle \hat{x}^2 \rangle - \langle \hat{x} \rangle^2, \tag{B2a}$$
$$\Delta^2 p = \langle \hat{p}^2 \rangle - \langle \hat{p} \rangle^2, \tag{B2b}$$
$$\Delta L = \langle \hat{L} \rangle - 2\langle \hat{x} \rangle \langle \hat{p} \rangle, \tag{B2c}$$

are quantum correlations. One can use the Lagrange method (LM) with the constraint $I_\Delta = \hbar^2/4$, or alternatively, one could apply the Karush–Kuhn–Tucker (KKT) conditions [49], which generalize LM to inequality constraints. In this case, $I_\Delta \geq \hbar^2/4$. Both methods offer an intuitive understanding of the problem, providing candidates for extrema of I that satisfy the inequality we are seeking. Nevertheless, neither method solves our problem entirely, as both provide necessary but not sufficient conditions for the existence of an extremum.

To formally demonstrate the desired result, we employ the Cauchy–Schwarz inequality.

Cauchy–Schwarz inequality. Let $\mathcal{H}$ be a Hilbert space with inner product $\langle \cdot, \cdot \rangle$. For any $u, v \in \mathcal{H}$, the Cauchy–Schwarz inequality states [50]

$$|\langle u, v \rangle|^2 \leq \langle u, u \rangle \cdot \langle v, v \rangle, \tag{B3}$$

with equality if, and only if, u and v are linearly dependent.

We consider the quantity $I - I_\Delta$, which can be simplified to

$$I - I_\Delta = x^2 P + p^2 X - xpL. \tag{B4}$$

We need to check that this expression is not negative. We observe that the first two terms are positive, while the third can turn $I - I_\Delta$ negative. To establish this contribution, we apply the inequality of the arithmetic-geometric mean, which states that for all numbers $a, b \geq 0$, we have $a + b \geq 2\sqrt{ab}$. This results in

$$x^2 P + p^2 X \geq 2|xp| \sqrt{PX}. \tag{B5}$$

On the other hand, we want to use the Cauchy-Schwarz inequality in the Hilbert space $\mathcal{H}$. To do this, we consider the normalized quantum state $|\psi\rangle$, and we define the following vectors:

$$u := \hat{x}|\psi\rangle, \qquad v := \hat{p}|\psi\rangle. \tag{B6}$$

The Cauchy–Schwarz inequality in $\mathcal{H}$ translates as

$$|\langle \psi | \hat{x}\hat{p} | \psi \rangle|^2 \leq \langle \hat{x}^2 \rangle \cdot \langle \hat{p}^2 \rangle = XP. \tag{B7}$$

Using the fact that $\hat{L} = \hat{x}\hat{p} + \hat{p}\hat{x}$ is Hermitian, we deduce

$$L = \langle \hat{L} \rangle = 2\,\mathrm{Re}\langle \hat{x}\hat{p} \rangle. \tag{B8}$$

Taking the absolute value of L, we obtain

$$|L| = |\langle \hat{x}\hat{p} + \hat{p}\hat{x} \rangle| = 2|\mathrm{Re}\langle \hat{x}\hat{p} \rangle| \leq 2|\langle \hat{x}\hat{p} \rangle| \leq 2\sqrt{XP}, \tag{B9}$$

so that

$$|xpL| \leq 2|xp|\sqrt{XP}. \tag{B10}$$

Combining the bounds (B5) and (B10), we conclude that

$$x^2P + p^2X \geq |xpL|, \tag{B11}$$

which implies

$$I - I_\Delta \geq 0, \tag{B12}$$

with equality if, and only if, $x = p = 0$.

Therefore, the Cauchy–Schwarz inequality in the Hilbert space justifies the inequality

$$I \geq I_\Delta \geq \frac{\hbar^2}{4}, \tag{B13}$$

and confirms that the global minimum of I under the constraint is attained by centered states that saturate the Schrödinger–Robertson uncertainty bound.

AIMS Press